Article

Design of Ejectors for High-Temperature Heat Pumps Using Numerical Simulations

Julian Unterluggauer [ID], Adam Buruzs [ID], Manuel Schieder [ID], Verena Sulzgruber [ID], Michael Lauermann [ID] and Christoph Reichl *[ID]

Austrian Institute of Technology, 1210 Vienna, Austria; julian.unterluggauer@ait.ac.at (J.U.);
adam.buruzs@ait.ac.at (A.B.); manuel.schieder@ait.ac.at (M.S.); verena.sulzgruber@ait.ac.at (V.S.);
michael.lauermann@ait.ac.at (M.L.)
* Correspondence: christoph.reichl@ait.ac.at

Abstract: Decarbonization of industrial processes by using high-temperature heat pumps is one of the most important pillars towards sustainable energy goals. Most heat pumps are based on the standard Carnot cycle which includes an expansion valve leading to irreversible dissipation and energetic losses. Especially for high-temperature applications, these losses increase significantly, and a replacement of the conventional throttle valve with an ejector, which is an alternative expansion device, for partial recovery of some of the pressure lost during the expansion, is investigated in this paper. However, designing such a device is complicated as the flow inside is subject to multiphase and supersonic conditions. Therefore, this paper aims to streamline an approach for designing ejectors for high-temperature heat pumps using numerical simulations. To showcase the application of the design procedure, an ejector, which is used to upgrade a standard cycle high-temperature heat pump with the synthetic refrigerant R1233zdE, is developed. To design the ejector heat pump, an interaction between a fast 1D design tool, a 1D heat pump cycle simulation, and a 2D CFD simulation is proposed. An ejector is designed for a sink temperature of 130 °C, which can potentially increase the COP of the heat pump by around 20%. Preliminary measurements at off-design conditions at 100 °C sink temperature are used to validate the design procedure. The pressure distribution inside the ejector is well captured, with relative errors around 4%. However, the motive nozzle mass flow was underpredicted by around 30%. To summarize, the presented approach can be used for designing ejectors of high-temperature heat pumps, although the numerical modeling has to be further developed by validation with experiments to improve the prediction of the motive mass flow.

Keywords: high-temperature heat pump; ejector technology; computational fluid dynamics

1. Introduction

Around 24% of the total heating and cooling requirements in the EU are subject to industrial processes [1]. In 2020, approximately 65% of the required heat was still supplied by burning fossil fuels [2]. As it is no secret that this contributes to global warming and threatens our fragile ecological system, it is of the utmost importance to act immediately. Industrial electrification is considered to be the solution to heat demand by integrating larger amounts of renewables into the system [3]. To reduce energy demand and increase efficiency, high-temperature heat pumps can be integrated. Most of them are based on the Carnot cycle, which is a well-known principle with limited space for efficiency improvements. However, its Achilles heel will always be the expansion valve where exergy

is converted to anergy, resulting in the requirement of additional exergy. To minimize this effect, ejector expansion devices must recover pressure before the compressor can be used. This technology is far from new, being proposed already in 1858 by Henry Giffard. At the beginning of the 20th century, steam jet ejectors experienced a wave of popularity in refrigeration systems for air conditioning large buildings [4]. These ejectors were later superseded by mechanical compressors, which led to a standstill in the development of steam-jet ejectors in the middle of the 20th century. Ejectors became the focus of research again at the end of the century, when advanced numerical methods also aided the design process and the prediction of performance in refrigeration cycles, as demonstrated by Kornhauser in 1990 [5]. Interest in this technology is steadily growing, especially for the use of CO_2 in refrigeration [6]. However, experimental and numerical investigations of ejectors are still far from providing a complete understanding of the complex physics involved. Evaporation during acceleration in the Laval nozzle, which involves nucleation and bubble growth at supersonic and transonic speeds, leads to severe challenges in the design process [7]. The design process of an ejector is complicated, and a proper evaluation of the geometry and estimation of the key performance factors to match the system parameters is necessary. To do so, numerical modeling can be used to analyze ejector performance. To obtain crucial ejector performance indicators, 1D modeling is suggested in the literature, while more accurate flow profiles and detailed investigations can be achieved by 2D or 3D computational fluid dynamics (CFD).

A relevant study about classical zero and 1D models for single-phase ejectors can be found in the work of Huang et al. [8]. They calculate primary nozzle choking with analytical formulas for ideal gas (single phase Laval nozzle), and the effects of frictional and mixing losses are taken into account with isentropic efficiency factors. They verified the calculations with experiments performed for the refrigerant R141b. For the primary and secondary flow mixing, the hypothesis of Munday and Bagster is used [9]. Elbel [10] reused an iterative model of Korhauser [5], where a mass flow rate ratio of the suction to total flow was iteratively determined. With the help of separate isentropic efficiencies for the motive and suction nozzle, and the diffuser, they laid down the widely used ejector efficiency formula. The empirical isentropic efficiency factors are used in several subsequent works [11,12]. These efficiency factors simplify the calculations, but do not explain how these factors depend on operating conditions. The one-dimensional ejector simulation of Banasiak and Hafner [13] solves the 1D mass momentum and energy equations as ordinary differential equations for the primary and secondary flows, which also eliminates the isentropic efficiencies as external parameters. They use a coaxial flow modeling of the double-flow passages (for the mixer and diffuser), and developed a delayed equilibrium model for the thermodynamic description of vaporization. With their model, they successfully reconstructed the experimental pressure profile of a two-phase ejector using R744 as refrigerant. The model was further refined by Wilhelmsen et al. [14], and extended by the delayed homogeneous relaxation model. They also validated the model with the results of CO_2 ejector measurements. An alternative method for quick assessment of ejector design was described by Ringstad et al. [15], who fitted a Gaussian process regressor to hundreds of converged CFD simulations of CO_2 ejectors. However, this is only possible if the CFD model is validated properly. For the application of ejectors with the working fluid CO_2, there are many studies suggesting different multiphase flow models. Fast equilibrium models [16], which led to higher mass flow discrepancies, and experimental calibrated nonequilibrium models [17] can close that gap further.

However, apart from CO_2, other working fluids behave differently, affecting the numerical modeling. Therefore, in terms of high-temperature heat pumps, the development is straight behind, as efficiency gains were overshadowed by the simple need to address

higher temperatures in the past. As an example, AIT and SINTEF investigated a butane heat pump system [18] using a built-in ejector supplying up to 130 °C for the heat sink. For the design of the ejector, a 1D approach was used at that time only. However, the COP improvements were countered by the efficiency loss of the reciprocating compressor operating outside its design point. As a further development, an approach to designing an ejector for a high-temperature heat pump using a combination of system simulation with a 1D code and a 2D CFD analysis is presented here. This paper is structured as follows. First, the methodology of the paper, describing 1D and 2D simulations, is presented in detail. Afterwards, the presented methodology is used to design an ejector for a high-temperature heat pump with the synthetic refrigerant R1233zd(E). This refrigerant is a hydrofluoroolefin (HFO) with ultra-low global warming potential (GWP) of 4.5, a critical point at 166 °C and 36 bar, which gives it high potential in future high-temperature heat pump applications. This design is presented in the results section together with an experimental validation for a part-load operating point.

2. Methodology

2.1. Design Approach

The design approach consists of the combination of three tools. First, a heat pump model is built using the modeling language Modelica. It starts with choosing a compressor model for the desired working conditions and is further specified by adding details like pressure losses. Then, a 1D design tool programmed in Python is used to test multiple geometries in a very short time (30–120 s runtime each). Then, a 2D CFD simulation with ANSYS Fluent is conducted on the most promising result of the 1D geometry, which takes about a runtime of 1 h to obtain the result. The process is shown in Figure 1.
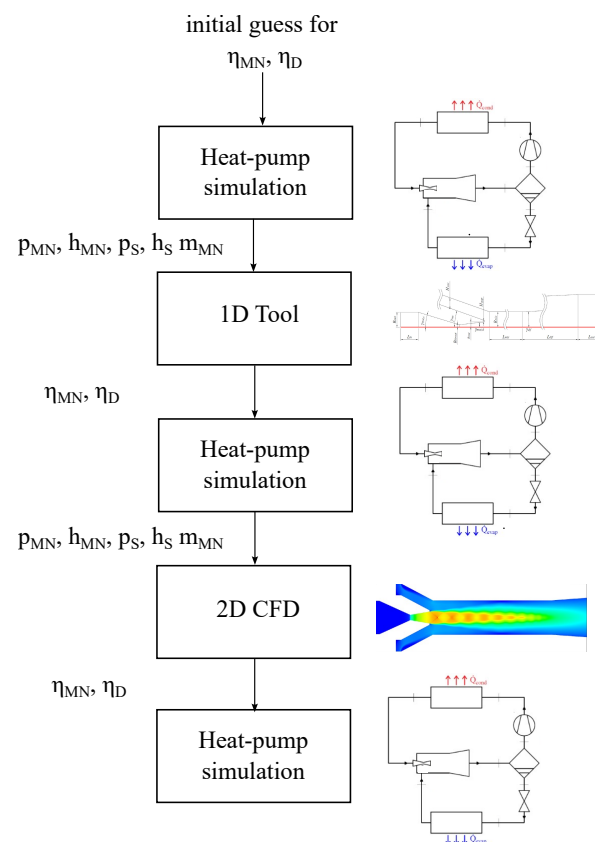
Figure 1. Design process.

2.2. 1D Ejector Heat Pump Model

Figure 2 shows a heat pump with an ejector. The ejector and separator divide the refrigeration cycle into the condensing and the evaporating circuit. Based on the pressure enthalpy diagram (see Figure 2b), the thermodynamic cycle can be described. A superheated fluid enters the compressor at stage 1 and is pressurized to 2. Then the heat is transferred to the water cycle by the condenser before the refrigerant enters an internal heat exchanger (IHEX) (3) to superheat the compressor inlet (1). Now, the subcooled refrigerant enters the ejector (4), mixes with the suction inlet (9), and leaves at a higher pressure level (5). A flash tank (separator) divides the circuit into the condenser loop, where the gaseous fluid (6) is moving to the IHEX, and the evaporator loop, where the liquid refrigerant (7) is heated up in the evaporator (9).

(a)	**(b)**
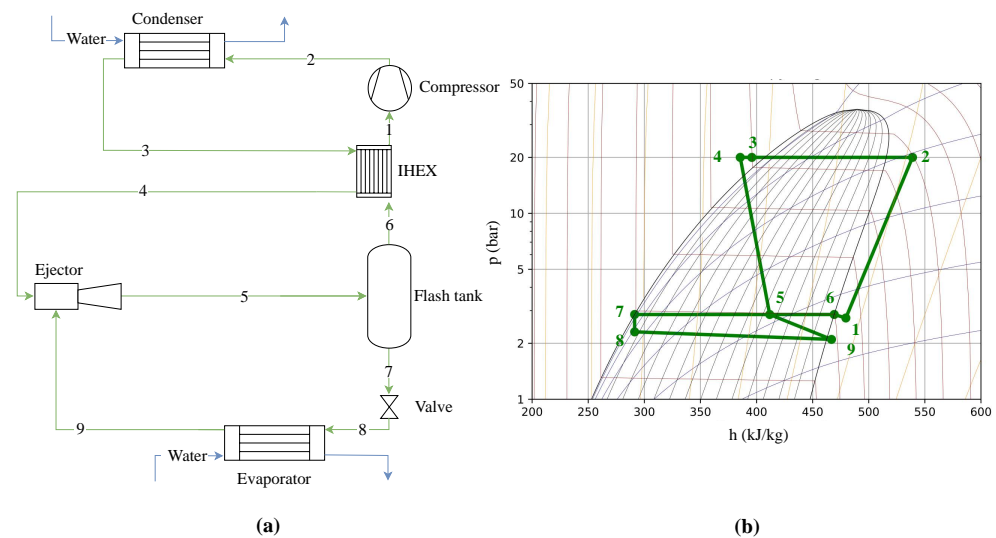
Figure 2. (**a**) Schema of the high-temperature heat pump with an ejector and an internal heat exchanger. (**b**) The corresponding p–h diagram. The pressure difference between points 5 (after the ejector diffuser) and 9 (ejector suction) is the pressure recovered by the ejector.

The heat pump cycle, including the required components such as the compressor and flash tank, is modeled using the acausal object-oriented, equation-based open-source modeling language Modelica.

The refrigeration circuit simulations were carried out using the TIL Library 3.10.0 (developed by TLK Thermo GmbH, Braunschweig, Germany) in the Dymola 2023x simulation environment. All components in the refrigeration circuit, such as the compressor, plate heat exchanger, expansion valve, and receiver, are based on the available models and were parameterized according to the manufacturer's specifications. Essentially, this is a 1D formulation that is discretized in the direction of the flow as required. The ejector, on the other hand, is a custom model developed by AIT that relies on the 0D formulation with the two efficiencies for the nozzle and the mixing chamber including diffuser. No geometry input is required here. The two efficiencies were compared and determined iteratively with the CFD analyses.

The thermophysical properties of the working media were taken from the fluid database in TILMedia, supplemented with the help of the tool REFPROP 10 [19]. The ejector model was programmed based on two independent isentropic efficiencies. The one for the motive nozzle is defined as

$$\eta_{MN} = \frac{h_{MN.in} - h_{MN.out}}{h_{MN.in} - h_{MN.out.is}} \tag{1}$$

and for the mixing part with the diffuser as

$$\eta_D = \frac{h_{MIX.in} - h_{D.out}}{h_{MIX.in} - h_{D.out.is}} \tag{2}$$

Those account for frictional losses and shock waves, for example. According to Figure 1, an initial guess for η_{MN} and η_D should be used. Liu et al. [20] summarized assumed ejector component efficiencies for refrigeration circuits in the literature. Based on that summary, one can assume $\eta_{MN} = 0.9$ and $\eta_D = 0.65$ as a first guess. According to Figure 1, the values will then be defined by the 1D approach similar to Kronhauser et al. [5], but also later on updated by values of the 2D CFD analysis.

The ejector efficiency

$$\eta_E = \frac{\dot{m}_{SN}}{\dot{m}_{MN}} \frac{h(s_{SN}, p_{D.out}) - h_{SN.in}}{h_{MN.in} - h(s_{MN}, p_{D.out})} \tag{3}$$

as defined by Elbel et al. [10] is often used in the literature to describe the whole ejector performance. This efficiency is defined as the ratio of the expansion work rate recovered by the ejector divided by the maximum possible expansion work rate recovery potential. To evaluate the performance of the heat pump, the so-called coefficient of performance,

$$COP = \frac{Q_{Sink}}{Q_{Source} + P_{el}}, \tag{4}$$

a ratio between the heating power of the sink (Q_{Sink}) and the sum of the heat source (Q_{Source}) and electrical power (P_{el}), is used. These equations are solved with the DASSL solver ([21]) as a transient simulation, where the steady-state operating conditions are reached asymptotically.

2.3. 1D Ejector Model

As first approximative estimations of ejector flow characteristics, zero- and one-dimensional models are often used in the literature [8,22]. In this study, an improved version of the numerical model of Buruzs et al. [23] was deployed, which is a combination of 1D and 0D models. In the 1D model, the radial variation of the flow field is neglected, and the flow equations are solved as ordinary differential equations along the symmetry axis. Therefore, by this approximation, the physical quantities are only functions of one spatial coordinate (x). The ejector is divided into several sections, where the solutions are searched separately: the primary nozzle, the secondary nozzle, the mixing chamber, and, lastly, the mixer and the diffuser. The governing equations express the mass, momentum, and energy conservation.

2.3.1. Primary Nozzle

For the 1D stationary flow, the conservation equations can be formulated in the following way. The mass conservation equation is expressed as a constant mass flow rate ($\dot{m}$), which can be calculated as the product of the density (ρ), flow velocity ($v(x)$), and the location dependent cross-section area of the primary nozzle ($A(x)$):

$$\dot{m} = \rho A v = const. \tag{5}$$

The differential form of the momentum equation can be written as follows (see Equation (2) of [13]):

$$-f\sqrt{\frac{\pi}{A}} \dot{m}\, v(x) = \dot{m}\frac{dv}{dx} + A\frac{dp}{dx} \tag{6}$$

Thereby, the viscous stress tensor is neglected, while the term on the left side, which corresponds to the friction with the wall, is taken into account with a simple coefficient of friction (f). This coefficient is analogous to the factor in the Darcy–Weisbach equation [24], which depends on the wall roughness, and Reynolds number, and should be around 0.01–0.05. The two terms on the right side are the standard momentum acceleration and pressure gradient. The energy conservation equation for the adiabatic case is given by the simple sum of the specific enthalpy (h) and velocity (v) terms (for derivation, see Chapter 4.3.3 of [24]):

$$h + \frac{v^2}{2} = const. \tag{7}$$

Within the homogeneous equilibrium (HEM) approximation, the fluid is considered to be in equilibrium in each position along the flow; thus, the density of the fluid is determined by the pressure and specific enthalpy:

$$\rho(x) = RP_\rho(p(x), h(x)), \tag{8}$$

using Refprop 10 [19] to obtain material properties, such as the density function RP_ρ.

Given the properties of the fluid flow at the inlet of the motive nozzle, the flow in the entire motive nozzle along its axis (x) can be calculated as the solution of (Equations (5)–(8)), so the problem is treated mathematically as an initial value problem of an ordinary differential system of equations. For the numerical solution, an implicit forward difference scheme is used, so that the mass conservation is exactly fulfilled at each discretization point x in space (until the nozzle throat). The discrete version of (Equations (5)–(8)) is the following equation system:

$$
\begin{aligned}
v_{i+1} &= \frac{\dot{m}}{A(x_{i+1})\rho_{i+1}} \\
-f\sqrt{\frac{\pi}{A(x_i)}}\frac{\dot{m}}{A(x_i)}v_i(\Delta x) &= \frac{\dot{m}}{A}(v_{i+1} - v_i) + (p_{i+1} - p_i) \\
0 &= \frac{(v_{i+1}+v_i)}{2}(v_{i+1} - v_i) + h_{i+1} - h_i \\
\rho_{i+1} &= RP_\rho(p_{i+1}, h_{i+1})
\end{aligned}
\tag{9}
$$

This equation system is nonlinear and solved as an implicit system of equations for each discrete grid point in the x direction for the updated velocity (v_{i+1}), pressure (p_{i+1}), and specific enthalpy (h_{i+1}) at the next point x_{i+1} using the Newton method. For the presented simulations, a fixed step size $\Delta x_i = x_{i+1} - x_i = 5.0 \times 10^{-5}$ m is used. If the inlet mass flow rate is below a critical value, the flow velocity increases until the throat but it does not reach the sonic velocity, and the velocity drops back in the divergent part of the nozzle. When the critical mass flow rate is reached, the flow switches to a supersonic solution at the throat, and the flow further accelerates until the exit of the divergent part. As the flow accelerates, the pressure decreases, and, as a result, a pressure difference to the suction inlet occurs so that mass flow from the secondary nozzle is sucked in. It is not possible to increase the inlet velocity (and mass flow rate) over this critical value; this phenomenon is called choking. Choking means, by our numerical solution, that if the inlet velocity v_0 is larger than the critical value v_{crit}, then Equation (9) does not have a real solution. In this case, there exists a point x_c before the nozzle exit where the numerical solution of the difference system Equation (9) fails within an error tolerance value (e.g., 10^{-3}). The critical mass flow is determined from the condition that it is the largest value at which the integration of the system of equations Equation (9) is still possible up to the nozzle exit. The failure of the solution of the system happens exactly at the critical mass flow rate value, where the flow reaches the sonic velocity. The value of this critical inlet velocity is determined with the bisection method, by iteratively dividing the interval between subsonic and overcritical

(nonconvergent) speed values by two until a given velocity accuracy tolerance is reached. It is often difficult to find the critical solution of the flow where the subsonic–supersonic transition happens at the throat. Therefore, an artificial velocity correction (usually around 0.1%) is applied at the throat of the nozzle so that the integrator jumps into the supersonic solution. The necessary pressure jumps are calculated from the mass flow conservation. This artificial jump (correction) of the solution introduces slight inaccuracies in the solution but enables us to find the required supersonic solution in the divergent part of the nozzle.

2.3.2. Pre-Mix Chamber

For the modeling of the pre-mixing region, the Munday–Bagster assumption [9] is used, i.e., until section Y (called the aerodynamic throat), the primary and secondary flows do not mix—that means that there is no mass or momentum exchange—and at Y, the two flows reach the same pressure niveau [25]. Huang et al. [8] assumed that the secondary flow chokes at this aerodynamic throat (also called the hypothetical throat, and referred to as Y; see Figure 2 of [8]), and this condition enabled them to calculate the secondary mass flow rate for this critical (double choking) operating mode. However, it is not required for the secondary flow to be choked (subcritical operating mode of the ejector). In this pre-mixing section, both flows have an isentropic expansion (or compression). For the primary and secondary flows, the mass, energy, and entropy conservation can be written in the following form:

$$\dot{m}_P = \rho_{P.Y} v_{P.Y} A_{P.Y} \qquad \dot{m} = \rho_{S.Y} v_{S.Y} A_{S.Y}$$

$$h_{MN.out} + \frac{v_{MN.out}^2}{2} = h_{P.Y} + \frac{v_{P.Y}^2}{2} \qquad h_{Stg} = h_{SN.in} + \frac{v_{SN.in}^2}{2} = h_{S.Y} + \frac{v_{S.Y}^2}{2}$$

$$\rho_{P.Y} = RP_\rho(p_{P.Y}, h_{P.Y}) \qquad \rho_{S.Y} = RP_\rho(p_{S.Y}, h_{S.Y})$$

$$s_{P.MN.out} = RP_S(p_{P.Y}, h_{P.Y}) \qquad s_{Stg} = RP_S(p_{S.Y}, h_{S.Y}) \qquad (10)$$

where h_{Stg} and s_{Stg} stand for stagnation specific enthalpy and entropy. The geometric constrain for cross-section of the primary and secondary flow at section Y is determined by their sum, which covers the whole mixer cross-sectional area (A_m):

$$A_m = A_{SY} + A_{PY} \qquad (11)$$

At the point Y, the primary and secondary pressure equal the following:

$$p_Y = p_{PY} = p_{SY} \qquad (12)$$

In the subcritical operating mode, when the secondary flow is not choked, an additional equation for the secondary flow is needed. Similarly to [26], the momentum equation for the secondary flow is added. The often complicated 3D shape of the secondary nozzle is reduced to an inlet area, and an approximative 1D momentum equation (friction and viscous effects are neglected) in the form of

$$\rho v \frac{dv}{dx} = -\frac{dp}{dx} \qquad (13)$$

is used. The equation is integrated from the suction inlet (S_i) until the Y-equalized pressure section for the secondary flow.

$$\int_{x_{SN.in}}^{Y} \rho v \frac{dv}{dx} dx = - \int_{x_{SN.in}}^{Y} \frac{dp}{dx} dx \qquad (14)$$

As the flow is treated as compressible, substitution is needed, and without using the exact geometry as a very rough approximation, the integral is replaced with the simplest trapezoid rule: $\int_a^b f(x)\,dx \approx (b-a)\frac{f(b)+f(a)}{2}$; therefore, we obtain an approximative momentum equation:

$$(\rho_{SN.in} + \rho_{SY})(v_{SY}^2 - v_{SN.in}^2) = 4(p_{SN.in} - p_{SY}) \tag{15}$$

Finally, the 10 Equations (10), (11), and (15) determine the 10 variables:

$$p_Y, v_{P.Y}, \rho_{P.Y}, h_{PY}, A_{P.Y}, v_{S.Y}, \rho_{SY}, h_{S.Y}, A_{S.Y}, \dot{m}_S \tag{16}$$

This set of equations is solved numerically with the SciPy Python package [27] multivariate root finder function, which uses the Levenberg–Marquardt algorithm of MINPACK.

2.3.3. Mixer Calculations

The primary and secondary flows enter the constant cross-section mixer. The mixing calculations are similar to the method developed by Banasiak and Hafner [13]. They consider the two flows (primary and secondary flow) as coaxial, having a common boundary surface where mass and momentum exchange takes place. According to [13], there are two types of mass transfer between the primary and secondary flows: Γ_c stands for the condensation mass transfer rate, and $\Gamma_{S\rightarrow P}$ for the mass transfer rate from secondary flow to primary flow. The sum of the two terms gives the mass transfer between the two flows:

$$\frac{d\dot{m}_{primary}}{dx} = -\frac{d\dot{m}_{secondary}}{dx} = \frac{d\Gamma_c}{dx} + \frac{d\Gamma_{s\rightarrow p}}{dx} \tag{17}$$

The mass flow rates can be expressed as the product of the density (ρ), velocity (v), and cross-section (A), so we obtain the following form:

$$\frac{1}{v_j}\frac{dv_j}{dx} + \frac{1}{\rho_j}\frac{\partial\rho}{\partial p}\frac{dp}{dx} + \frac{1}{\rho_j}\frac{\partial\rho_j}{\partial h}\frac{dh_j}{dx} + \frac{1}{A_j}\frac{dA_j}{dx} = i_j\frac{1}{v_j\rho_j A_j}\left(\frac{d\Gamma_c}{dx} + \frac{d\Gamma_{s\rightarrow p}}{dx}\right) \tag{18}$$

$$\text{with } j \in (s, p) \text{ and } \quad i_j = \begin{cases} 1 & \text{for the primary flow } (j = P) \\ -1 & \text{for the secondary flow } (j = S) \end{cases} \tag{19}$$

The momentum equation takes the following form:

$$A_j\frac{dp}{dx} + A_j\rho_j v_j\frac{dv_j}{dx} = i_j(v_s - v_p)\frac{d\Gamma_{s\rightarrow p}}{dx} - i_j\frac{d\Pi}{dx} \tag{20}$$

where Π is the rate of momentum exchange, and the additional friction force between the two flows and the friction on the ejector wall is neglected. The energy equation:

$$A_j\rho_j v_j^2\frac{dv_j}{dx} + A_j\rho_j v_j\frac{dh_j}{dx} = i_j\left[h_s - h_j + \frac{1}{2}\left(v_s^2 - v_p^2\right)\right]\frac{d\Gamma_{s\rightarrow p}}{dx} + \delta_{j,s}\frac{dQ_w}{dx} \tag{21}$$

$\frac{dQ_w}{dx}$ is the heat exchange between the wall and the secondary flow. The total cross-section of the mixer (A) means a geometrical constrain for the cross sections of the primary (A_p) and secondary flow (A_s):

$$\frac{dA_s}{dx} + \frac{dA_p}{dx} = \frac{dA}{dx} \tag{22}$$

These equations have to be solved for the quantities ($p, v_p, v_s, h_p, h_s, A_p, A_s$) with the given geometry (specified $\frac{dA(x)}{dx}$ function). For the mass transfer rate $\frac{d\Gamma_{S\rightarrow p}}{dx}$, an approximation is required. It is assumed that it has a linear dependency on the flow velocity:

$\frac{d\Gamma_{s\to P}}{dx} = \beta_{sp}v_pR_p2\pi$, where $R_p = \sqrt{A_p/\pi}$ is the radius of the primary flow cylinder. For the momentum exchange rate $\frac{d\Pi}{dx}$, we use the resistance formula as an approximation using the speed difference of the two flows:

$$\frac{d\Pi}{dx} = \beta_{drag}(v_p - v_s)^2 2R_p\pi\,\text{sign}(v_p - v_s) \tag{23}$$

where β_{sp}, β_{drag} are parameters to be determined from experiments.

2.3.4. Implementation

The solution of the numerical equations listed in this section was implemented in Python programming language, and the source code is published on github (https://github.com/AdamBuruzs/simpy_ejector, accessed on 24 December 2024) and also available in the Python package index (pip (https://pypi.org/, accessed on 24 December 2024)) as the *simpy_ejector* package.

2.4. 2D CFD Model

2.5. Multiphase Modeling

The accuracy of the simulations is strongly influenced by the robustness and accuracy of the multiphase modeling approach. Therefore, the HEM based on the studies of Smolka et al. [16] and Giacomelli et al. [28] is widely used. This model assumes a thermal and mechanical equilibrium between the liquid and gaseous phases, simplifying the governing equations to their single-phase formulation. To use this model, the energy equation must be solved in its enthalpy-based form. Since ANSYS Fluent uses the temperature-based energy equation, the enthalpy-based formulation needs to be implemented as a user-defined scalar:

$$\nabla \cdot (\rho\tilde{u}\tilde{h}) = \nabla \cdot (\Lambda_h\nabla\tilde{h}) + S_{h1} + S_{h2} + S_{h3}, \tag{24}$$

with Λ_h being the diffusivity of the enthalpy (*h*).

$$\Lambda_h = \frac{\lambda}{c_p} + \frac{\mu_t}{Pr_t} \tag{25}$$

In Equation (25), λ denotes the thermal conductivity, c_p the specific heat capacity, μ_t the turbulent viscosity, and Pr_t the turbulent Prandtl number. The source term S_{h1} represents the mechanical energy, S_{h2} the irreversible dissipation of kinetic energy variations, and S_{h3} the dissipation of turbulent kinetic energy. The exact form of the s used in this study is published by Schieder et al. [29]. However, with subcritical motive nozzle pressures and in a subcooled state, the HEM approach leads to an underprediction of the motive nozzle mass flow rate and stability problems [30]. Therefore, the homogeneous relaxation model (HRM) can be used to account for meta-stable effects. The model originates from the basics of refrigeration modeling conducted by Einstein [31], and is based on a linearized expansion proposed by Bilicki et al. [32].

In this approach, the relaxation time is used to calculate the actual vapor quality, taking nonequilibrium phase change into account, as described by Downar-Zapolski et al. [33]. The actual vapor quality can be defined as

$$\frac{\partial(\rho\overline{X})}{\partial t} = \rho\frac{\overline{X}_{equ} - \overline{X}}{\theta} \tag{26}$$

with $\overline{X}$ as the instantaneous vapor mass fraction affected by the metastability, $\overline{X}_{equ}$ as its equilibrium value, and θ as the relaxation time. This relaxation time is then defined by

$$\theta = \theta_0 \alpha^a \phi^b \tag{27}$$

according to Downar-Zapolski et al. [33], based on the Moby Dick experiments for water. Thereby,

$$\alpha = \frac{\overline{X}\overline{\rho}}{\rho_{sat}} \tag{28}$$

is the void fraction. For higher pressures (>10 bar), Angielczyk et al. [34] set the constant $\theta_0 = 2.14 \times 10^{-7}$ s, $a = -0.54$, and $b = -1.76$, respectively. The nondimensional pressure difference

$$\phi = |\frac{\overline{p}_{sat}(s_{MN}) - \overline{p}}{p_{crit} - \overline{p}_{sat}(s_{MN})}| \tag{29}$$

is adapted for fluids closer to the critical point, targeting specifically CO_2. As no specific parameters are mentioned in the literature for R1233zd(E) and the conditions are more similar to the CO_2 application (distance to the critical point), it was decided to use the parameters suggested by Angielczyk et al. [34]. As the last step, ρ and h of the mixture must be computed again in the following equations:

$$\rho = \frac{1}{\frac{\overline{X}}{\rho_{sat}} + \frac{1-\overline{X}}{\rho(p,h_{ml})}} \tag{30}$$

$$h = \overline{X}h_{sat}(p) + (1 - \overline{X})h_{ml} \tag{31}$$

However, in the absence of a stable HEM solution, the HRM approach cannot be utilized, as it requires a converged vapor quality determined by the HEM. One method to artificially enhance stability when an HEM solution is unavailable involves recalculating the HEM solution at every iteration. Based on these updated HEM results, the HRM solution is computed iteratively. This contrasts with the classical HRM approach, where the HEM solution is held constant throughout the process. Due to the high degree of subcooling, a stable HEM solution could not be obtained; therefore, this iterative approach is implemented.

2.6. Setup

The CFD simulation case is set up as a 2D domain using ANSYS Fluent 2023R2 for steady-state simulations. The governing equations are briefly described in the theory guide [35] of the software. The energy equation is solved in the enthalpy-based form to set up the multiphase flow model. An additional transport equation for the enthalpy is then solved by using a user-defined scalar (UDS). Moreover, the material properties are updated by calling a user-defined function (UDF), which performs a bilinear interpolation to obtain material properties as functions of the pressure (p) and specific enthalpy (h) based on the REFPROP 10.0 database [19]. To model turbulence, the $k - \omega$-SST model [36] with enhanced wall functions is used. All equations are solved using first-order upwind schemes, except for pressure, where a second-order upwinding interpolation scheme is chosen. The domain is meshed using ANSYS 2023R2 Workbench to generate a full hexahedral grid (see Figure 3) with the values depicted in Table 1. A grid independence study was performed as part of the diploma thesis of Manuel Schieder [37]. Alongside the investigation of the required number of cells, a comparison between 2D and 3D CFD is presented.

Table 1. Grid parameters.

Quantity	Value
Number of cells	383,520
Determinant	0.96
Maximum screwness	0.5
y^+_{ave}	2.2
y^+_{max}	9.5
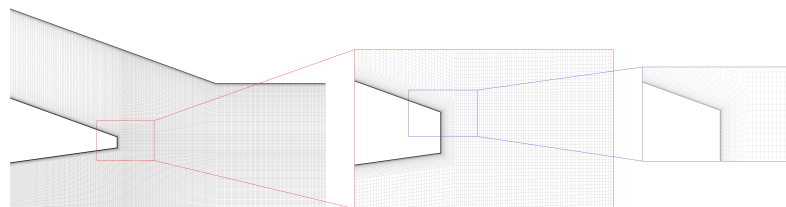
Figure 3. Mesh of the ejector. The boundary layer in the primary nozzle and the rest of the ejector has a thickness of 0.3 mm. Whereas this length is divided into 50 cells with a growth rate of 1.101 for the ejector, it is divided into 20 cells with a growth rate of 1.129 for the rest of the ejector.

3. Results

3.1. Design Point

Table 2 shows the desired operating conditions for the heat pump. As refrigerant, the new-generation HFO R1233zd(E) is chosen. It is currently not targeted by the HFO phase-down regulations and is classified in safety category A1 according to the European standard [38] for indicating its nonflammability and nontoxicity. Together with the moderate pressure levels for high-temperature HPs (<25 bar), this is beneficial in terms of specific safety measures or special strength requirements of the materials used. Source and sink temperatures are chosen based on the compressor model, and the heating capacity is selected based on the capacity of a laboratory test stand for experimental validation.

Table 2. Design conditions.

Quantity	Value
Refrigerant	R1233zd(E)
Source	Water, 45 °C
Sink	Pressurized water, 130 °C
Heating capacity	60 kW

The final ejector geometry is shown in Table 3 according to the sketch depicted in Figure 4.

Table 3. Ejector geometry.

Quantity	Unit	Value
R_{TH}	mm	2.4
$R_{MN.in}$	mm	14.0
$R_{MN.out}$	mm	7.5
$\gamma_{MN.c}$	°	7.0
$\gamma_{MN.d}$	°	6.0
R_{MIX}	mm	14.6
L_{MIX}	mm	110
L_D	mm	255.0
γ_D	°	2
L_{TOTAL}	mm	573
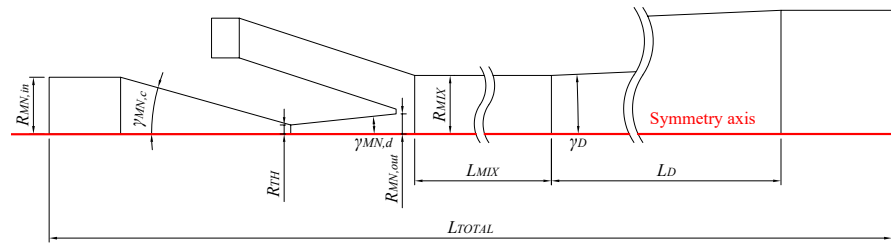
Figure 4. Geometry of the designed ejector.

Table 4 shows the result of the heat pump simulation. The ejector has an efficiency of around 26% by increasing the compressor inlet pressure by approximately 1.3 bar.

Table 4. Operating point of the design case.

Quantity	Unit	Value
COP	-	2.04
η_{MN}	-	0.96
η_D	-	0.44
η_E	-	0.26
$p_{MN.in}$	bar	19.99
$p_{SN.in}$	bar	2.09
$h_{MN.in}$	$\frac{\text{kJ}}{\text{kg}\cdot\text{K}}$	354.2
$h_{SN.in}$	$\frac{\text{kJ}}{\text{kg}\cdot\text{K}}$	435.2

Figure 5 shows the results depicted in Table 4 compared to the standard cycle. The final ejector design can increase the COP by around 20% to a value of 2.04. Moreover, the heating power increases by 25% with a lower hot gas temperature based on the decreased pressure ratio.
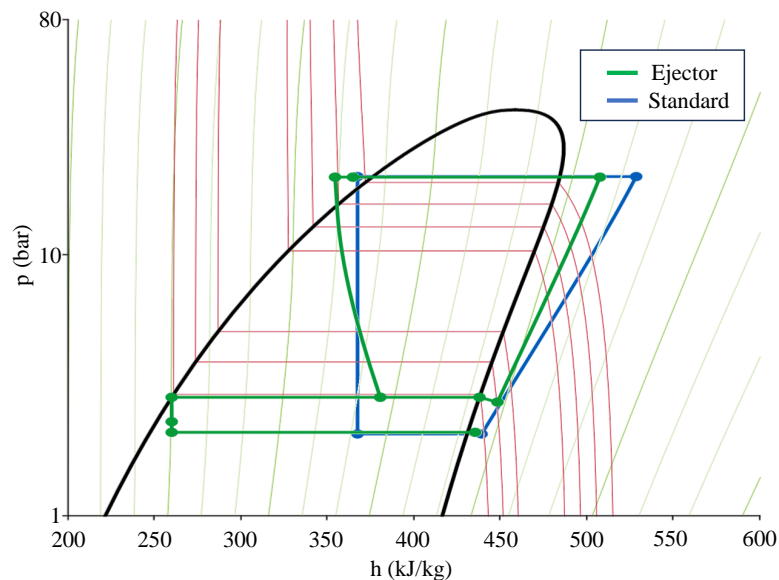
Figure 5. Comparison between the standard cycle and the results with the ejector.

Figure 6 compares the pressure distribution of the 1D tool to the 2D CFD. The CFD results distinguish between those close to the wall where pressure measurement sensors would have been mounted ($p_{CFD.wall}$) and values taken at the axis ($p_{CFD.ax}$). Within the Laval nozzle part, the pressure distribution of the 1D is similar to the 2D results, with a difference of around 10% at the outlet. On the right-hand side of Figure 6, the pressure recovery in the mixing chamber and the diffuser is displayed. On the axis, the pressure

oscillates downstream of the motive nozzle outlet due to the formation of shockwaves; this is graphically displayed in Figure 7. Contrary to the wall pressure, the shockwave crossing the axis leads to an abrupt change in pressure.
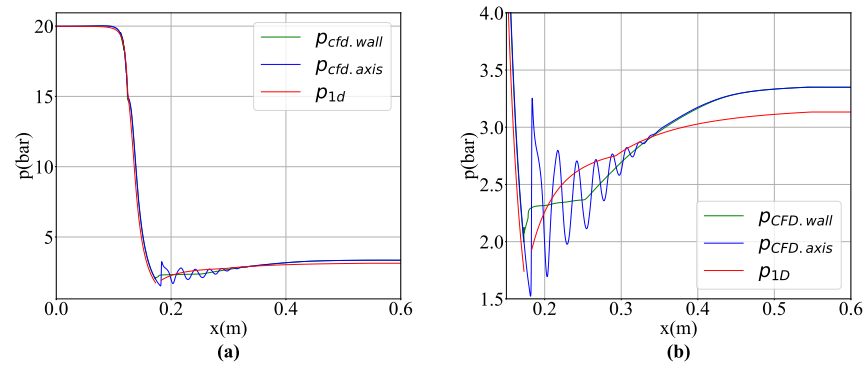
Figure 6. Comparison between 1D and 2D CFD simulation in the design point. (**a**) Pressure distribution in the whole ejector. (**b**) The part after the motive nozzle.

Figure 7 shows a contour plot of the Mach number. In the convergent part of the motive nozzle, the Mach number increases to a value of 1 at the throat and then reaches supersonic conditions in the divergent part of the nozzle.
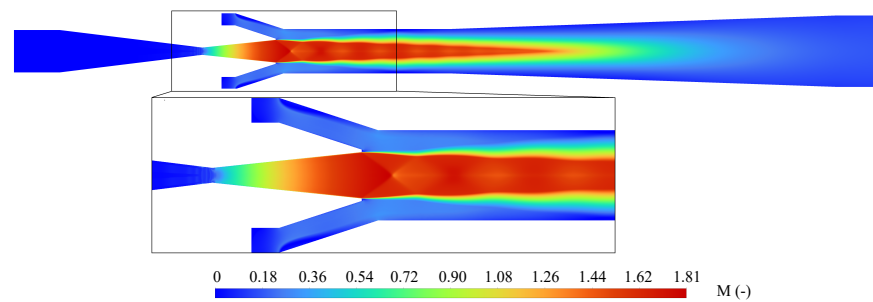
Figure 7. Mach number of the ejector in the design point.

When leaving the motive nozzle, the typical shock pattern forms, resulting in the appearance of so-called Mach diamonds, which are displayed in Figure 8. The angle of the shockwave (γ_{shock}) is around 35 °,while the length of the shockwave (L_{shock}) is approximately 10 mm. In the mixing zone, a sharp boundary between the motive and suction nozzle flow can be seen, which diffuses over the length of the mixing zone and vanishes shortly after the diffuser entrance. The flow reaches a subsonic state on nearly the whole cross-section at the beginning of the diffuser. Only a small area around the axis is still supersonic. This is required because the flow needs to be mostly subsonic to recover pressure in the diffuser.
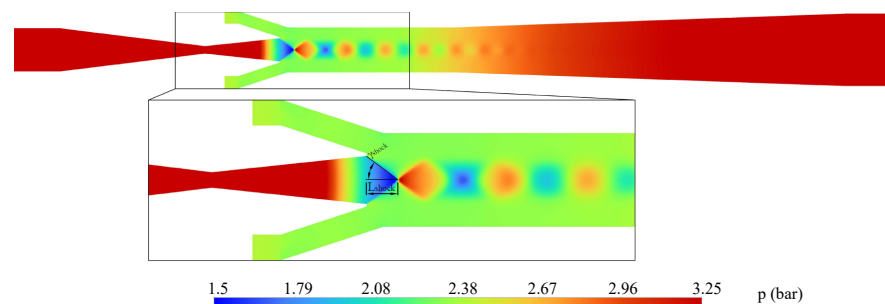
Figure 8. Contour plot of pressure distribution of the ejector in the design point showing shock behavior and Mach diamonds.

The primary nozzle flow is calculated with 1D simulation, as described in Section 2.3.1, and the CFD model. The resulting mass flow values are depicted in Table 5. In the 1D simulation, a critical inlet velocity of 0.71 $\frac{\text{m}}{\text{s}}$ resulted in a primary mass flow rate of 0.548 $\frac{\text{kg}}{\text{s}}$. The mass flow rate predicted by the 2D CFD simulation was around 12% higher, while the suction mass flow rates differed from each other by just approximately 1%.

Table 5. Design point mass flows.

Quantity	Value
$\dot{m}_{1D.MN}$ $\left(\frac{\text{kg}}{\text{s}}\right)$	0.548
$\dot{m}_{CFD.MN}$ $\left(\frac{\text{kg}}{\text{s}}\right)$	0.618
$\dot{m}_{1D.SN}$ $\left(\frac{\text{kg}}{\text{s}}\right)$	0.305
$\dot{m}_{CFD.SN}$ $\left(\frac{\text{kg}}{\text{s}}\right)$	0.309

3.2. Validation

A test rig was designed, and a first measurement campaign had already been carried out. However, based on the available test rig infrastructure, only temperatures of 100 °C were possible. Nevertheless, this operating point is displayed in Table 6 and can be used to validate the ejector design procedure. Five differential pressure sensors are mounted in the ejector to validate its pressure recovery. Additionally, pressure and temperature are measured at the motive nozzle inlet, diffuser outlet, and the suction inlet. The instrumental approach and the campaign itself are documented in [39].

Table 6. Ejector conditions at the measured operating point.

Quantity	Unit	Value
$p_{MN.in}$	bar	10.39
$p_{S.in}$	bar	2.47
$h_{MN.in}$	$\frac{\text{kJ}}{\text{kg·K}}$	354.5
$h_{S.in}$	$\frac{\text{kJ}}{\text{kg·K}}$	466.6

The ejector design is displayed in Figure 9. To stabilize operation towards higher mass flows, a suction bypass according to Bodys et al. [40] was implemented. However, the bypass was closed during the first measurement campaign because the heat pump was running in part-load and it was originally designed to handle higher mass flows.
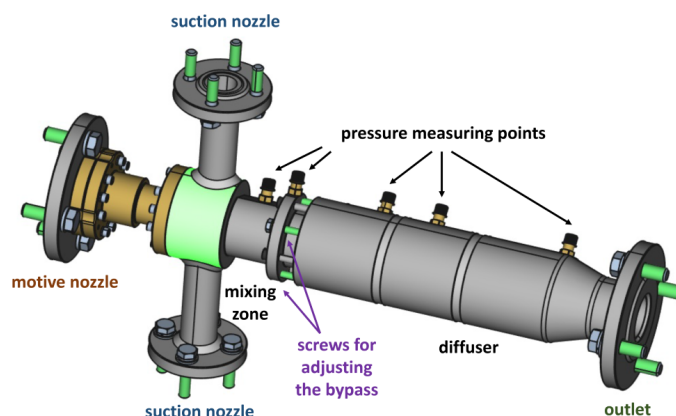
Figure 9. 3D model of the ejector built for the measurements.

Figure 10 shows the pressure distribution in the ejector. The results of the 1D and 2D simulations are compared to the pressure measurements. Relative pressure sensors are

used with a maximum uncertainty of 0.1%. As absolute values are displayed in Figure 10b, the reference accuracy of 0.1% is added on top of those [39]. It can be seen that the overall distribution of the pressure is well captured by the model.
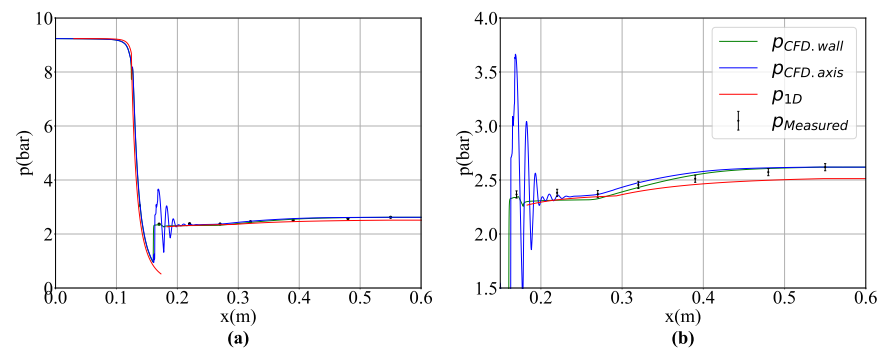
Figure 10. Validation point pressure distribution (**a**) of the whole ejector and (**b**) of the mixing section and diffuser, including measurement uncertainty.

Figure 11 shows the Mach number resulting from the CFD simulation at the measurement operating point. The simulation predicts that the shock occurs much earlier in the divergent part of the nozzle compared to the design point (Figure 8). This leads to a much worse performance of the Laval nozzle. It has also to be mentioned that the steady solution never fully converges, hinting at the occurrence of unsteady flow behavior. In addition, it can be concluded that the ejector is not working properly, as pressure rises by only around 4%, compared to the 60% increase in the design point. However, it can be seen that the numerical modeling captures the overall behavior of the ejector well. The 2D CFD tool reaches a relative error value of approximately 2.3%, while the 1D tool predicts the pressure at the outlet with a discrepancy of around 4%.
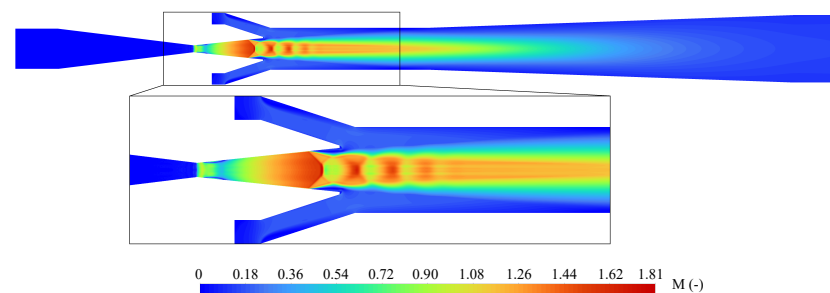
Figure 11. Mach number from the CFD simulation at the measurement point.

Table 7 shows the mass flow rates of the 1D and the 2D simulation compared to the measured mass flows. In the experiment, the motive and suction mass flow rates are measured by Coriolis sensors with an uncertainty of $\pm 0.2\%$ [39]. The motive mass flow is severely underpredicted by the 1D approach by around 40% and the 2D CFD by approximately 30%. For the suction mass flow, the 1D method shows a 50% discrepancy, while with the 2D CFD method, it differs by only around 14%. The low accuracy of the 1D model can also be explained by the rough zero-dimensional estimation of the suction nozzle flow (Section 2.3.2), where an isentropic flow is assumed without an external efficiency parameter. The relatively high deviation of the predicted mass flows from the real values is already mentioned in the literature for CO_2 ejectors.

Table 7. The mass flow rates by the measured operating point.

Quantity	Unit	Value
$\dot{m}_{1D.MN}$	$\frac{kg}{s}$	0.192
$\dot{m}_{CFD.MN}$	$\frac{kg}{s}$	0.22
$\dot{m}_{EXP.MN}$	$\frac{kg}{s}$	0.31
$\dot{m}_{1D.SN}$	$\frac{kg}{s}$	0.32
$\dot{m}_{CFD.SN}$	$\frac{kg}{s}$	0.14
$\dot{m}_{EXP.SN}$	$\frac{kg}{s}$	0.16

4. Conclusions and Outlook

An approach to streamline the development of a high-temperature heat pump ejector was presented. The approach contains a combination of heat pump system simulation, 1D ejector simulations, and a detailed 2D CFD model. The idea was to efficiently deal with the multiple challenges in the design phase of such a device by exploiting the advantages of every tool. To validate the procedure, an ejector for a high-temperature heat pump with the synthetic refrigerant R1233zd(E) was designed. The heat pump itself should deliver 130 °C with a heating capacity of 60 kW based on a 45 °C water source. Based on the results of the numerical calculation, an ejector design was found that could potentially increase the COP of this heat pump by around 20%. A first measurement campaign underlined the reliability of the design approach. The pressure distribution in the ejector mixing zone and the diffuser was well captured, with a maximal error of 4% even under part-load conditions. However, the motive mass flow was severely underpredicted by the 1D approach by around 40% and by the 2D CFD by approximately 30%. For the suction mass flow, the 1D method showed a 50% discrepancy, while with the 2D CFD method, it differed by only around 14%. The relatively high deviation of the predicted mass flows from the real values is already mentioned in the literature for CO_2 ejectors. To further validate the procedure and the implemented numerical models, experiments in the design point are planned after an necessary upgrade of the test rig infrastructure. Moreover, we also plan to investigate the part-load behavior of the ejector using the designed bypass.

Nomenclature

Acronyms

CFD	Computational fluid dynamics
GGI	General grid interface
IHEX	Internal heat exchanger
HEM	Homogeneous Equilibrium Model
HRM	Homogeneous Relaxation Model
HEX	Heat exchanger
RP	Refprop Materials library functions [19]

Abbreviations

α	Void fraction $(-)$
γ	Angle $(°)$
Λ_h	Diffusivity of h $(\frac{kg}{s \cdot m})$
λ	Thermal conductivity $(\frac{W}{m \cdot K})$
ρ	Density $(\frac{kg}{m^3})$
ϕ	Nondimensional pressure difference $(-)$
Γ	Mass transfer rate $(\frac{kg}{s})$
Π	Momentum transfer rate $(\frac{kg \cdot m}{s})$
W	Force (N)
η	Efficiency $(-)$
∇	Nabla operator $(\frac{1}{m})$
μ	Viscosity $(\frac{kg}{s \cdot m})$
A	Cross-section (m^2)
a	Coefficient of the HRM model $(-)$
b	Coefficient of the HRM model $(-)$
c_p	Specific heat capacity $(\frac{J}{kg})$
COP	Courant–Friedrichs–Lewy number (-)
f	Friction factor (-)
h	Specific enthalpy $(\frac{J}{kg})$
L	Length (m)
$\dot{m}$	Mass flow $(\frac{kg}{s})$
p	Pressure (bar)
Pr	Prantl number $(-)$
R	Radius (m)
s	Entropy $(\frac{kg \cdot m^2}{s^2 \cdot K})$
T	Temperature $(°C)$
v	Velocity $(\frac{m}{s})$
y^+	Dimensionless wall distance $(-)$
x	x-direction (m) along the symmetry axis of the ejector
$\overline{X}$	Steam content (-)
y	y-direction (m)

Subscripts

crit	Critical point
D	Diffuser
E	Ejector
el	Electric
equ	Equilibrium
i	Counter
in	Inlet
is	Isentropic
out	Outlet
P	Primary flow

MIX	Mixing zone
MN	Motive nozzle
ml	Meta stable
S	Secondary flow
SN	Suction nozzle
Stg	Stagnation point
sat	Saturation point
shock	Shockwave
TH	Throat
t	Turbulent
Y	Hypothetical/aerodynamic throat

References

1. European Commission. A Clean Planet for All. A European Strategic Long-Term Vision for a Prosperous, Modern, Competitive and Climate Neutral Economy. 2018. Available online: https://eur-lex.europa.eu/legal-content/EN/TXT/?uri=celex:52018DC0773 (accessed on 24 December 2024).
2. Eurostat. Gross and Net Production of Electricity and Derived Heat by Type of Plant and Operator. Online Data Code: nrg_ind_peh. Available online: https://ec.europa.eu/eurostat/databrowser/product/page/NRG_IND_PEH (accessed on 24 December 2024).
3. Schüwer, D.; Schneider, C. Electrification of industrial process heat: Long-term applications, potentials and impacts. In Proceedings of the Leading the Low-Carbon Transition: ECEEE Industrial Summer Study, Berlin, Germany, 11–13 June 2018; Proceedings; Europ. Council for an Energy Efficient Economy: Stockholm, Sweden, 2018; pp. 411–422.
4. Chunnanond, K.; Aphornratana, S. Ejectors: Applications in refrigeration technology. *Renew. Sustain. Energy Rev.* **2004**, *8*, 129–155. [CrossRef]
5. Kornhauser, A.A. The use of an ejector as a refrigerant expander. In Proceedings of the USNC/IIR-Purdue Refrigeration Conference, Purdue University, West Lafayette, IN, USA, 17–20 July 1990.
6. Elbel, S.; Lawrence, N. Review of recent developments in advanced ejector technology. *Int. J. Refrig.* **2016**, *62*, 1–18. [CrossRef]
7. Giacomelli, F.; Mazzelli, F.; Banasiak, K.; Hafner, A.; Milazzo, A. Experimental and computational analysis of a R744 flashing ejector. *Int. J. Refrig.* **2019**, *107*, 326–343. [CrossRef]
8. Huang, B.J.; Chang, J.M.; Wang, C.P.; Petrenko, V.A. A 1-D analysis of ejector performance. *Int. J. Refrig.* **1999**, *22*, 354–364. [CrossRef]
9. Munday, J.T.; Bagster, D.F. A New Ejector Theory Applied to Steam Jet Refrigeration. *Ind. Eng. Chem. Process Des. Dev.* **1977**, *16*, 442–449 . [CrossRef]
10. Elbel, S.; Hrnjak, P. Experimental validation of a prototype ejector designed to reduce throttling losses encountered in transcritical R744 system operation. *Int. J. Refrig.* **2008**, *31*, 411–422. [CrossRef]
11. Zhou, M.; Wang, X.; Yu, J. Theoretical study on a novel dual-nozzle ejector enhanced refrigeration cycle for household refrigerator-freezers. *Energy Convers. Manag.* **2013**, *73*, 278–284. [CrossRef]
12. Mastrowski, M.; Smolka, J.; Butrymowicz, D.; Antczak, Ł.; Gagan, J.; Śmierciew, K. Experimental validation of the theoretical ejector model in a low-grade waste heat refrigeration system using R1233zdE as a working fluid. *Appl. Therm. Eng.* **2024**, *236*, 121716. [CrossRef]
13. Banasiak, K.; Hafner, A. 1D Computational model of a two-phase R744 ejector for expansion work recovery. *Int. J. Therm. Sci.* **2011**, *50*, 2235–2247. [CrossRef]
14. Wilhelmsen, Ø.; Aasen, A.; Banasiak, K.; Herlyng, H.; Hafner, A. One-dimensional mathematical modeling of two-phase ejectors: Extension to mixtures and mapping of the local exergy destruction. *Appl. Therm. Eng.* **2022**, *217*, 119228. [CrossRef]
15. Ringstad, K.E.; Banasiak, K.; Ervik, Å.; Hafner, A. Machine learning and CFD for mapping and optimization of CO_2 ejectors. *Appl. Therm. Eng.* **2021**, *199*, 117604. [CrossRef]
16. Smolka, J.; Bulinski, Z.; Fic, A.; Nowak, A.J.; Banasiak, K.; Hafner, A. A computational model of a transcritical R744 ejector based on a homogeneous real fluid approach. *Appl. Math. Model.* **2013**, *37*, 1208–1224. [CrossRef]
17. Bodys, J.; Smolka, J.; Palacz, M.; Haida, M.; Banasiak, K. Non-equilibrium approach for the simulation of CO_2 expansion in two-phase ejector driven by subcritical motive pressure. *Int. J. Refrig.* **2020**, *114*, 32–46. [CrossRef]
18. Schlemminger, C.; Kopp, C.; Banasiak, K.; Drexler-Schmid, G.; Lauermann, M.; Windholz, B.; Zauner, C.; Baumhakel, A. Hochtemperatur Wärmepumpe mit Ejektor. In Proceedings of the DKV Tagung 2019, Ulm, Germany, 20–22 November 2019.

19. Lemmon, E.W.; Bell, I.H.; Huber, M.L.; McLinden, M.O. *NIST Standard Reference Database 23: Reference Fluid Thermodynamic and Transport Properties-REFPROP, Version 10.0*; National Institute of Standards and Technology: Gaithersburg, MD, USA, 2018. [CrossRef]

20. Liu, F.; Groll, E.A. Study of ejector efficiencies in refrigeration cycles. *Appl. Therm. Eng.* **2013**, *52*, 360–370. [CrossRef]

21. Petzold, L.R. *Description of DASSL: A Differential/Algebraic System Solver*; Number: SAND-82-8637; Sandia National Laboratories: Albuquerque, NM, USA, 1982.

22. Grazzini, G.; Milazzo, A.; Mazzelli, F. *Ejectors for Efficient Refrigeration: Design, Applications and Computational Fluid Dynamics*; Springer: Cham, Switzerland, 2018.

23. Buruzs, A.; Marx, K.; Lauermann, M.; Zenz, C.; Barz, T.; Reichl, C. Ejektoren für Wärmepumpen-Grobauslegung mittels 1D Strömungssimulation. In Proceedings of the Deutsche Kälte und Klimatagung, Online , 19–20 November 2020; Deutsche Kälte- und Klimatagung: Dresden, Germany, 2020.

24. Oertel, H. (Ed.) *Prandtl-Essentials of Fluid Mechanics*; Applied Mathematical Sciences; Springer: New York, NY, USA, 2010; Volume 158. [CrossRef]

25. He, S.; Li, Y.; Wang, R.Z. Progress of mathematical modeling on ejectors. *Renew. Sustain. Energy Rev.* **2009**, *13*, 1760–1780. [CrossRef]

26. Djajadiwinata, E.; Sadek, S.; Alaqel, S.; Orfi, J.; Al-Ansary, H. Numerical and One-Dimensional Studies of Supersonic Ejectors for Refrigeration Application: The Significance of Wall Pressure Variation in the Converging Mixing Section. *Appl. Sci.* **2021**, *11*, 3245. [CrossRef]

27. Virtanen, P.; Gommers, R.; Oliphant, T.E.; Haberland, M.; Reddy, T.; Cournapeau, D.; Burovski, E.; Peterson, P.; Weckesser, W.; Bright, J.; et al. SciPy 1.0: Fundamental algorithms for scientific computing in Python. *Nat. Methods* **2020**, *17*, 261–272. [CrossRef]

28. Giacomelli, F.; Mazzelli, F.; Milazzo, A. Evaporation in supersonic CO_2 ejectors: Analysis of theoretical and numerical models. In Proceedings of the International Conference on Multiphase Flow, Firenze, Italy, 22–27 May 2016.

29. Schieder, M.; Zenz, C.; Unterluggauer, J.; Lauermann, M.; Buruzs, A.; Wilk, V.; Fleckl, T.; Reichl, C. Characterization of the fluid flow phenomena in an ejector for a high temperature heat pump. In Proceedings of the the 14th IEA Heat Pump Conference, The Royal Society London, Chicago, IL, USA, 15–18 May 2023.

30. Bodys, J.; Smolka, J.; Palacz, M.; Haida, M.; Banasiak, K.; Nowak, A.J. Effect of turbulence models and cavitation intensity on the motive and suction nozzle mass flow rate prediction during a non-equilibrium expansion process in the CO_2 ejector. *Appl. Therm. Eng.* **2022**, *201*, 117743. [CrossRef]

31. Einstein, A. Uber Schallschwingungen in teilweise dissoziierten Gasen. *Sitz. Berl. Akad. Phys. Chem.* **1920**, *380*.

32. Bilicki, Z.; Kestin, J. Physical aspects of the relaxation model in two-phase flow. *Proc. R. Soc. London. A. Math. Phys. Sci.* **1990**, *428*, 379–397.

33. Downar-Zapolski, P.; Bilicki, Z.; Bolle, L.; Franco, J. The non-equilibrium relaxation model for one-dimensional flashing liquid flow. *Int. J. Multiph. Flow* **1996**, *22*, 473–483. [CrossRef]

34. Angielczyk, W.; Bartosiewicz, Y.; Butrymowicz, D.; Seynhaeve, J.M. 1-D modeling of supersonic carbon dioxide two-phase flow through ejector motive nozzle. In Proceedings of the International Refrigeration and Air Conditioning Confernce, Purdu University, West Lafayette, IN, USA, 12–15 July 2010.

35. ANSYS, Inc. *Ansys® Fluent Theory Guide, Release 2023 R2*; ANSYS, Inc.: Canonsburg, PA, USA, 2023.

36. Menter, F.R.; Kuntz, M.; Langtry, R. Ten years of industrial experience with the SST turbulence model. *Turbul. Heat Mass Transf.* **2003**, *4*, 625–632.

37. Schieder, M. Characterization and Optimization of Ejectors using Numerical Fluid Dynamics. Master's Thesis, TU Wien, Wien, Austria, 2023. [CrossRef]

38. *EN 378-1:2016+A1:2020 (E)*; Refrigerating Systems and Heat Pumps—Safety and Environmental Requirements, Part 1 Basic Requirements, Definitions, Classification and Selection Criteria. BSI: London, UK, 2020; pp. 1–80.

39. Stöger, L. Experimental Characterisation of a High-Temperature Heat Pump with Ejector. Master's Thesis, TU Wien, Vienna, Austria, 2024.

40. Bodys, J.; Smolka, J.; Palacz, M.; Haida, M.; Banasiak, K.; Nowak, A.J. Experimental and numerical study on the R744 ejector with a suction nozzle bypass. *Appl. Therm. Eng.* **2021**, *194*, 117015. [CrossRef]